

Crater wear prediction in turning Ti6Al4V considering cutting temperature effect

Kejia Zhuang

Ming Li

Fengtian Lin

Cheng Hu

Jian Weng

Zhongmei Gao (✉ zhongmei12345@126.com)

Huazhong University of Science and Technology

Chaoqun Wu

Research Article

Keywords: Crater wear, Cutting temperature, Turning, Ti6Al4V

Posted Date: March 8th, 2022

DOI: <https://doi.org/10.21203/rs.3.rs-1414352/v1>

License: © ⓘ This work is licensed under a Creative Commons Attribution 4.0 International License.

[Read Full License](#)

Crater wear prediction in turning Ti6Al4V considering cutting temperature effect

Kejia Zhuang ^{a,b}, Ming Li ^a, Fengtian Lin ^c, Cheng Hu ^a, Jian Weng ^a, Zhongmei Gao ^{a,b,*}, Chaoqun Wu ^a

^a Hubei Digital Manufacturing Key Laboratory, School of Mechanical and Electronic Engineering, Wuhan University of Technology, Wuhan 430070, China

^b State Key Laboratory of Digital Manufacturing Equipment and Technology, Huazhong University of Science and Technology, Wuhan 430074, China

^c Xiamen Golden Egret Special Alloy Corporation Limited, Xiamen 361000, China

Abstract: Tool wear has great impacts on tool life and cutting parameter selection in the machining process. As ceramic inserts are widely employed in efficient machining, it is of great significance to predict accurately the wear of ceramic tools. Crater wear is one of the most significant tool wear modes when turning difficult-to-cut materials at high speeds. The purpose of this research is to demonstrate the forming and influence mechanisms of crater wear in Ti6Al4V turning with ceramic inserts while considering cutting temperature at the tool-chip interface. An effort is made to describe quantitatively the appearance of crater wear from the perspective of temperature distribution based on crater wear experiments under various cutting conditions. In order to obtain the cutting temperature distribution efficiently, an analytical temperature prediction model is used in this paper. Then a prediction model for crater wear depth and width considering the influence of the maximum temperature is developed. The maximum crater wear depth and width models are validated by a series of cutting experiments, and the outcomes prove that the proposed models are practical. Additionally, the influence of various cutting parameters on crater wear is discussed. The cutting speed has the greatest impact on crater wear, followed by the feed rate. Furthermore, this research can be used to improve cutting parameters for controlling crater wear.

Keywords: Crater wear; Cutting temperature; Turning; Ti6Al4V

E-mail address: zhongmei12345@126.com

Nomenclature

| | |
|---------------------------------|--|
| K_T | the maximum depth of crater wear |
| K_B | the maximum width of crater wear |
| T_{max} | the maximum temperature value at the tool-chip interface |
| V_c | cutting speed |
| F_t | feed rate |
| a_p | cutting depth |
| DMZ | dead metal zone |
| PDZ | the primary deformation zone |
| SDZ | the secondary deformation zone |
| q_{pr}, q_{se}, q_d | intensity of the heat source in the primary deformation zone, secondary deformation zone and dead metal zone, respectively |
| A_0, B_0, C_0, n_0, m_0 | material constants |
| T_m, T_r | melting temperature and room temperature |
| σ | shear strain |
| $d\sigma$ | shear strain rate |
| $d\sigma_0$ | reference shear strain rate |
| V_s | shear velocity |
| V_{ch} | chip flow velocity |
| V_m | DMZ velocity |
| τ_s, τ_m, τ_c | local shear flow stresses |
| θ | slip-line angle |
| γ | rake angle |
| ϕ | shear angle |
| ϕ_s | immersion angle |
| η_r | chip flow angle on the rake plane |
| ξ_1, ξ_2 | friction factor angle |
| θ_c | addition of chamfer angle |
| α_0 | initial rake angle |
| α_n | local rake angle |
| l_m | side length of the dead metal zone |
| l_c | side length of the secondary heat source |
| l_s | side length of the primary heat source |
| w | cutting width |
| B_{tool} | dynamic heat distribution coefficient of the heat sources on the tool side |
| B_{chip} | dynamic heat distribution coefficient of the heat sources on the chip side |
| $B_c, B_t, \Delta B, C_1, m, k$ | adjusting factors |
| S_0, K_0 | constant coefficients |
| α_w, λ_w | thermal diffusivity and conductivity of workpiece |
| α_t, λ_t | thermal diffusivity and conductivity of tool |
| α | angle of crater wear |
| R | radius of crater wear |
| S | volume of crater wear |

1. Introduction

Titanium alloy is widely applied to many fields, such as biomedical, aerospace, automotive, and chemical industries, owing to its excellent biocompatibility, good toughness, and high fatigue endurance at high temperatures [1]. Meanwhile, it is considered to be a material that is particularly difficult to process due to the following characteristics: high strength, low thermal conductivity and easily adhering to the tool surface during cutting [2]. During turning Ti6Al4V with coated cemented carbide tools, it is found that high cutting temperature concentrates at the tool-chip interface adjacent to the cutting edge, where the highest temperature can exceed 1000°C, accelerating the formation of wear [3, 4]. This restricts cutting speed and feed speed, and thus reduces the machining efficiency of titanium alloy. As a result, high-speed turning tactics with ceramic inserts are progressively used by manufacturers due to their high temperature resistance and wear resistance. Nevertheless, severe tool wear still happens because of the poor processability of titanium alloy. Crater wear on the rake face is the most important failure mechanism in the machining process of Ti6Al4V [5].

A slew of studies have been conducted on the formation mechanisms of the crater wear during machining Ti6Al4V using carbide tools. Experimental research has been the most common principal method for crater wear analysis. Venugopal et al. [3] noted that adhesion-dissolution-diffusion wear resulted in the crater wear during machining Ti6Al4V with uncoated carbide cutting inserts under cryogenic cooling. Similar findings were observed by Liang et al. [6] while turning Ti6Al4V with WC-10Ni3Al and WC-8Co carbide tools. In high-speed end-milling Ti6Al4V with uncoated cemented tungsten carbide inserts, Zhang et al. [7] stated that adhesion and diffusion were the predominant tool wear mechanisms in milling Ti6Al4V. Many studies indicated that the high temperature generated on the rake face caused co element diffusion from tool to workpiece, weakening the tool and accelerating crater wear [8-12]. To further study tool wear, some efforts have been devoted based on analytical models and the finite element method (FEM). Usui et al. [13] investigated the process of wear development based on the wear characteristic equation. It was found that the projected wear progress and tool life and the experimental findings were in good accordance. Malakizadi et al. [14] put forward a FEM-based method for predicting the evolution rate of the flank wear during turning operations. Thepsonthi and Özel [15]

predicted the tool wear and life employing FEM with DEFORM software, and concluded that the CBN coated carbide tool was superior to the uncoated carbide tool during micro-milling of Ti6Al4V. A crater wear prediction method based on dimensional analysis and FEM simulation with DEFORM-2d software was proposed by Ramírez et al. [16], which described the tool wear rate considering the combined effect of different thermo-mechanical wear mechanisms acting on the tool-chip interface.

On the basis of crater wear studies, cutting temperature on the rake face has a vital impact on crater wear during turning Ti6Al4V [11]. Norihiko [17] investigated the cutting temperature during titanium alloy machining, and experimentally concluded that the serious tool wear was mainly caused by high cutting temperature. Usui et al. [13] regarded the temperature at the contact surface as one of the decisive variables to establish a wear model based on the equation of adhesive wear. Molinari and Nouari [18] found that the temperature-sensitive diffusion process had the strongest effect on the wear rate, particularly at higher cutting speeds. Sun et al. [19, 20] studied the crater wear patterns of carbide tools and discovered that pressure and temperature had a significant impact on the wear rate when turning Ti6Al4V. To give a clear description, available wear models developed in the previous studies considering temperature variable are summarized in Table 1.

Table 1 Available wear models considering temperature variable (σ_n : normal stress, v_{sl} : average sliding velocity, T_{int} : contact temperature, t : cutting time)

| References | Wear model | Model overviews |
|--------------------------|---|---|
| Usui [13] | $\dot{w} = k \sigma_n v_{sl} \exp\left(-\frac{\alpha}{T_{int}}\right)$ | Wear rate was predicted considering σ_n , v_{sl} and T_{int} on the wear surface. |
| Malakizadi et al. [14] | $\dot{w} = k v_{sl} \exp\left(-\frac{B}{T_{int}}\right)$ | Wear rate was predicted considering v_{sl} and T_{int} on the flank wear faces. |
| Ramírez et al. [16] | $\dot{K}_T = k_1 \left(\frac{\sigma_n T_{int}^7}{4 \sqrt{v_{sl}^3}} \right)^{-k_2} t^{k_3}$ | Crater wear depth was predicted considering σ_n , v_{sl} , T_{int} , t and $(\sigma_n, v_{sl}, T_{int})$ were calculated from the 2D finite element model. |
| Molinari and Nouari [18] | $K_T = k_1 \sum_{i=1}^n \left[\frac{\sqrt{\frac{t}{\pi}} D_{i1}(T_{int}(x))}{(C_{i1}^0 - C_{i2}^0)} \right]$ | Crater wear depth was predicted considering σ_n , v_{sl} , T_{int} , t based on diffusion wear mechanism and diffusion was dominated by contact temperature. |
| Sun et al. [19, 20] | $\ln \left(\frac{k_1 \dot{w}}{\sigma_n v_{sl}} \right) = \ln k - \frac{\alpha}{T_{int}}$ | Wear rate was predicted considering σ_n , v_{sl} , T_{int} and the change of temperature had a great effect on the wear volume. |

From the research mentioned above, numerous investigations have been conducted about the crater wear in machining Ti6Al4V from experimental and simulation methods, however, few studies have been reported on the prediction of crater wear profile considering the influence of tool-chip interface temperature distribution applying analytical models when machining Ti6Al4V with ceramic round inserts.

The primary purpose of this work is to demonstrate the forming and influence mechanisms of crater wear considering cutting temperature at the tool-chip interface in the turning of Ti6Al4V with ceramic inserts. A quantitative prediction model for the crater wear is proposed, including the maximum depth of crater wear (K_T) and width of crater wear (K_B), based on an analytical cutting temperature model. By inputting different sets of cutting parameters into the analytical cutting temperature model, the corresponding maximum temperature value and the temperature distribution along the longest contact length can be obtained. Thereby, a crater wear prediction model is established based on the maximum temperature at the tool-chip interface. Finally, the model is validated by experiments under a broad range of T_{max} . The effects of cutting speed (V_c), feed rate (F_t) and cutting depth (a_p) on crater wear are analyzed based on

this prediction model. Then a suitable combination of cutting parameters is proposed to decrease crater wear, and thus promote machining efficiency in turning Ti6Al4V.

This paper consists of six sections. Section 1 summarizes the research on the wear behavior during machining Ti6Al4V. The detailed experimental settings are described in Section 2. An analytical cutting temperature model is elaborated and experimental results are analyzed in Section 3. A prediction model for crater wear considering the temperature distribution at the tool-chip interface is presented in Section 4, followed by model verification and discussion in Section 5. Conclusions are drawn in Section 6.

2. Experiments

A set of turning experiments were carried out in this section under dry cutting conditions. Fig. 1 shows the machining center and devices used in the experiment. The cutting experiments were performed on a three-axis CK6180 lathe, as given in Fig. 1a. Fig. 1b and Fig. 1c depict the tool holder (CRSNR 2525M 12-ID) and the round ceramic insert (RNG 45T6015 650) used in this work, respectively. The digital microscopy system (KEYENCE VHX-970F) served to extract data from the crater surface to form three-dimensional graphics and measure the profiles of crater wear, as shown in Fig. 1d.

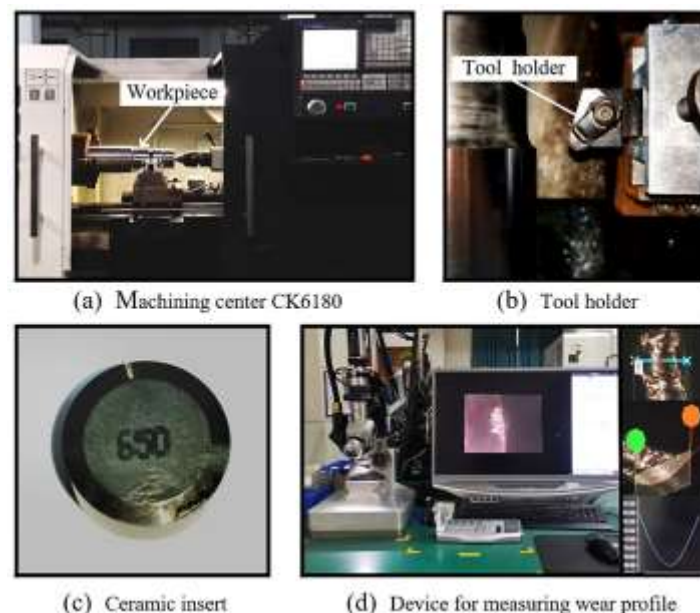


Fig. 1. Experimental setup for turning of Ti6Al4V with ceramic inserts.

Table 2 shows the chemical composition of the Ti6Al4V cylindrical workpiece. The hardness and density of the workpiece are approximately 36 HRC and 4430 kg/m³,

respectively. The solid cylindrical workpiece with 120 mm diameter and about 200 mm long was turned with round ceramic tools. The material of the tool is the most advanced Si_3N_4 , which belongs to the professional category of high-temperature refractories and shows splendid impact strength, wear performance and heat resistance. It is suitable for processing difficult-to-cut alloys. In the tool manufacturer's recommendation manual, this sort of cutting insert is frequently utilized for high-speed cutting of titanium alloys. The geometry information of the insert is shown in Table 3.

Table 2 The chemical composition of the workpiece (wt. %) [21].

| C | Fe | N | O | Al | V | H | Ti |
|------|------|------|------|----|---|-------|---------|
| 0.03 | 0.10 | 0.01 | 0.15 | 6 | 4 | 0.003 | Balance |

Table 3 Geometric parameters of the cutting tool.

| | |
|---------------|----------|
| Diameter | 12.7 mm |
| Thickness | 7.938 mm |
| Chamfer angle | 15° |
| Flank angle | 0° |
| Chamfer width | 1.5 mm |

The cutting settings were configured as roughing operation in dry cutting mode during the cutting process. Each experiment was repeated three times under the identical conditions and the measurement results were the average of the three experiments. A L9 (3^4) orthogonal array was established to investigate the impact of cutting depth (a_p), cutting speed (V_c) and feed rate (F_t) on crater wear, as shown in Table 4. Experiments Nos. 1-9 were carried out. In view of rapid tool wear in the case of high-speed turning of Ti6Al4V, the cutting stroke remained a small constant for all the experiments.

Table 4 The orthogonal experiment parameters.

| No. | a_p /mm | V_c /(m/min) | F_t /(mm/rev) |
|-----|-----------|----------------|-----------------|
| 1 | 0.5 | 75 | 0.1 |
| 2 | 0.75 | 75 | 0.125 |
| 3 | 1 | 75 | 0.15 |
| 4 | 1 | 90 | 0.125 |
| 5 | 0.75 | 90 | 0.1 |
| 6 | 0.5 | 90 | 0.15 |
| 7 | 0.5 | 105 | 0.125 |
| 8 | 0.75 | 105 | 0.15 |
| 9 | 1 | 105 | 0.1 |

3. Analytical cutting temperature model

In cutting experiments, it is difficult to measure precisely the temperature distribution at the tool-chip interface by experimental methods [22]. Many studies have shown that FEM simulation is able to effectively deal with non-linear problems such as material and thermal-mechanical coupling [23, 24], while its efficiency is insufficient. In this section, an analytical cutting temperature model based on Johnson-Cook's material constitutive law was proposed to calculate the temperature distribution at the cross-section perpendicular to the primary cutting edge and throughout the location of the K_T during turning Ti6Al4V. The model can provide a fairly accurate cutting temperature prediction with a substantially reduced computing cost compared with FEM simulation. Then, the maximum temperature values for experiments Nos. 1-9 were obtained by the temperature model for analysis of variance (ANOVA). Furthermore, a series of cutting experiments are designed to obtain different cutting temperatures according to the results of analysis of variance.

3.1 Cutting temperature model

Hu et al. [25] studied the three-dimensional temperature field during turning, and proposed an analytical model for predicting the temperature distribution at the tool-chip interface. Then the presented model was validated by a succession of finite element simulations and cylindrical turning experiments. The approach for determining the related heat sources, as well as the geometry and dynamical analysis of turning, were developed in our prior work [26, 27]. Due to plastic deformation and friction, it is generally assumed that four principle heat sources coexist in the process of metal

$$\begin{cases} V_{ch} = \frac{V_c \sin(\phi)}{\cos(\xi_2)} \\ V_s = V_c \cos(\phi) + V_{ch} \sin(\xi_2) + V_c \sin(\phi) \theta \\ V_m = \frac{V_c \sin(\xi_1 - \varepsilon)}{\sin(\xi_1)} \end{cases} \quad (4)$$

where A_0 , B_0 , C_0 , n_0 and m_0 stand for yield strength, strength coefficient, strain rate sensitivity coefficient, strain hardening exponent and thermal softening coefficient of the workpiece, respectively. Shear strain, shear strain rate and the reference shear strain rate are represented by σ , $d\sigma$ and $d\sigma_0$, respectively. T_r and T_m are the room temperature and melting temperature, respectively. ξ_1 and ξ_2 are the determined friction factor angles, ε is the angle between V_c and V_m , ϕ stands for the shear angle, as shown in Fig. 2.

Table 5 The Johnson-Cook parameters for Ti6Al4V [28].

| A_0/MPa | B_0/MPa | C_0 | n_0 | m_0 | T_r/K | T_m/K |
|------------------|------------------|--------|-------|-------|----------------|----------------|
| 896 | 656 | 0.0128 | 0.5 | 0.8 | 293 | 1993 |

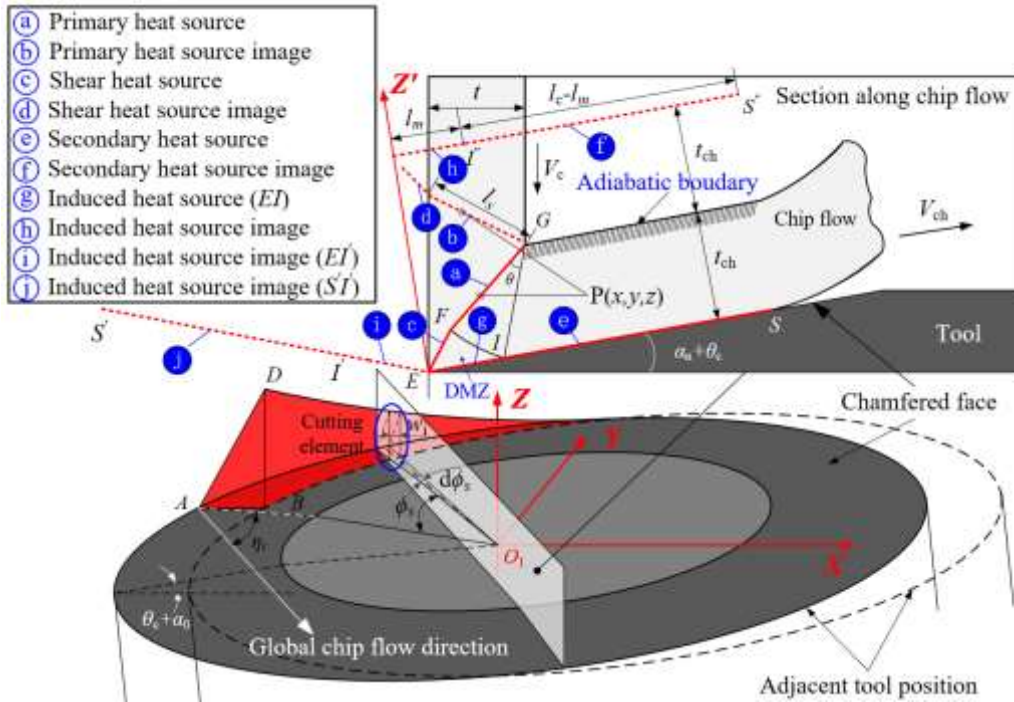


Fig. 3. Distribution of heat sources with relevant images.

The temperature rise of the chip (T_{Mchip}) was impacted by a combination of eight heat sources labeled by a~h in Fig. 3, which can be formulated as follow:

$$T_{\text{Mchip}} = \begin{cases} \frac{q_{\text{pr}}}{2\pi\lambda_w} \int_{l_i=0}^{l_s} e^{(Y-l_m \sin(\alpha_n + \varepsilon + \theta_c) - l_i \sin(\phi + \alpha_n + \theta_c)) V_{\text{ch}} / 2\alpha_w} K_0 \left(\frac{V_{\text{ch}}}{2\alpha_w} \right) (R_1 + R_1') dl_i \\ + S_0 \frac{q_d}{2\pi\lambda_w} \int_{l_i=0}^{l_m} e^{(Y-l_i \sin(\alpha_n + \varepsilon + \theta_c)) V_{\text{ch}} / 2\alpha_w} K_0 \left(\frac{V_{\text{ch}}}{2\alpha_w} \right) (R_2 + R_2') dl_i \\ + \frac{S_0 B_{\text{chip}} q_d}{\pi\lambda_w} \int_{l_i=0}^{l_m} e^{(Y-l_i) V_{\text{ch}} / 2\alpha_w} K_0 \left(\frac{V_{\text{ch}}}{2\alpha_w} \right) (R_3 + R_3') dl_i \\ + \frac{B_{\text{chip}} q_{\text{se}}}{\pi\lambda_w} \int_{l_i=l_m}^{l_c} e^{(Y-l_i) V_{\text{ch}} / 2\alpha_w} K_0 \left(\frac{V_{\text{ch}}}{2\alpha_w} \right) (R_4 + R_4') dl_i \end{cases} \quad (5)$$

where $R_1 \sim R_4$ and $R_1' \sim R_4'$ are the distance variables for the eight heat sources (a~h). α_n is the local rake angle, θ_c is the addition of chamfer angle. These angles are shown in Fig. 3. Y stands for the Y-axis coordinate value of point P. S_0 and K_0 are constant coefficients. The constants α_w and λ_w are the thermal diffusivity and conductivity of the workpiece. B_{chip} is the dynamic heat partition coefficient of heat sources on the chip side of the tool-chip contact face, which can be determined by Eq. (6).

$$B_{\text{chip}} = (B_c - \Delta B) + 2\Delta B \left(\frac{l_c - l_i}{l_c} \right)^m + C_1 \Delta B \left(\frac{l_c - l_i}{l_c} \right)^k \quad (6)$$

where B_c , ΔB , C_1 , m and k are adjustment factors that accurately match the temperature rise on both sides.

The exponential Y in Eq. (5) is the corrected coordinate value of point P (x, y, z) on the Y' axis, where the original Cartesian system X-Y-Z has been converted to X'-Y'-Z', and point E is the center of the transformed coordinate system. The three-dimensional coordinate transformation matrix was used to get the coordinate values of point P in the new system as follows:

$$U = \begin{bmatrix} \cos(\phi_s + \eta_r) & \sin(\phi_s + \eta_r) & 0 \\ -\sin(\phi_s + \eta_r) & \cos(\phi_s + \eta_r) & 0 \\ 0 & 0 & 1 \end{bmatrix} \begin{bmatrix} x + r \cos(\phi_s) \\ y - r \sin(\phi_s) \\ z + l_c \sin(\theta_c) \end{bmatrix} \quad (7)$$

$$\begin{bmatrix} X \\ Y \\ Z \end{bmatrix} = U * \begin{bmatrix} \cos(\alpha_n + \theta_c) & 0 & -\sin(\alpha_n + \theta_c) \\ 0 & 1 & 0 \\ \sin(\alpha_n + \theta_c) & 0 & \cos(\alpha_n + \theta_c) \end{bmatrix} \quad (8)$$

where ϕ_s is the immersion angle, η_r is the chip flow angle on the rake plane.

The temperature of the tool was generated by a combination of four heat sources labeled by e, g, I and j in Fig. 3, which can be calculated by:

$$T_{M_{\text{tool}}} = (1 - S_0) \frac{B_{\text{tool}} q_d}{2\pi\lambda_t} \int_{x_i=0}^{x_i=w} dy_i \int_{l_i=0}^{l_m} \left(\frac{1}{R_5} + \frac{1}{R_5'} \right) dl_i dx_i$$

$$+ \frac{B_{\text{tool}} q_{se}}{2\pi\lambda_t} \int_{x_i=0}^{x_i=w} dy_i \int_{l_i=l_m}^{l_c} \left(\frac{1}{R_6} + \frac{1}{R_6'} \right) dl_i dx_i$$
(9)

where R_5 , R_6 , R_5' and R_6' are the distances from point P to the four heat sources (e, g, i, j) respectively. w is the contact width between the tool cutting edge and the workpiece. λ_t is the thermal conductivity of the tool. Table 6 lists the mechanical properties of Si_3N_4 and Ti6Al4V applied in the proposed model. B_{tool} is the dynamic heat partition coefficient of heat sources on the tool side of the chip-tool contact face, which can be expressed by:

$$B_{\text{tool}} = (B_t + \Delta B) - 2\Delta B \left(\frac{l_c - l_i}{l_c} \right)^m - C_1 \Delta B \left(\frac{l_c - l_i}{l_c} \right)^k$$
(10)

where B_t is an adjustment factor that accurately matches the temperature rise on both sides of the tool-chip contact face.

According to the investigation of Huang et al. [29], the temperature of point P can be ultimately calculated by considering the thermal effects of every related heat source as below:

$$T_p = \sum_{j=1}^{j=n} T_{P_j} + T_r$$
(11)

where n is the number of the total heat sources.

Table 6 Mechanical properties of Ti6Al4V and Si_3N_4 [25,30].

| Material | Ti6Al4V | Si_3N_4 |
|----------------------|---|---|
| Thermal Conductivity | 7.4 W/(m·K) | 54.5 W/(m·K) |
| Thermal Diffusivity | $2.64 \times 10^{-6} \text{ W} \cdot \text{m}^2/\text{J}$ | $2.43 \times 10^{-5} \text{ W} \cdot \text{m}^2/\text{J}$ |

3.2 Temperature model validation

The temperature distribution results obtained from the analytical cutting temperature model and FEM simulation are compared in Fig. 4. Fig. 4a depicts the temperature field at the tool-chip interface by AdvantEdge (Version 7.1). Fig. 4b was obtained through the analytical cutting temperature model by MATLAB 2018a. Comparing the two results, it can be observed that the temperature distribution obtained using the analytical cutting temperature model matches well with the FEM simulation. Temperature profile from the FEM simulation (blue line) is compared with the result

from the proposed model (red line) in Fig. 4c to illustrate a clear comparison of the temperature distribution. The temperature profile was extracted along the longest contact length. It can be observed that the two temperature curves are in good agreement.

In terms of calculation time, it took much more time for FEM simulation compared with the proposed analytical model. It took about four hours to obtain a stable cutting state using 4 cores in parallel for the professional cutting simulation software AdvantEdge, while it only cost 567 seconds for the analytical model calculated by MATLAB 2018a using i5-7300HQ processor. Therefore, compared with FEM simulation, the analytical model can significantly improve calculation efficiency and reduce the computational cost with the same accuracy.

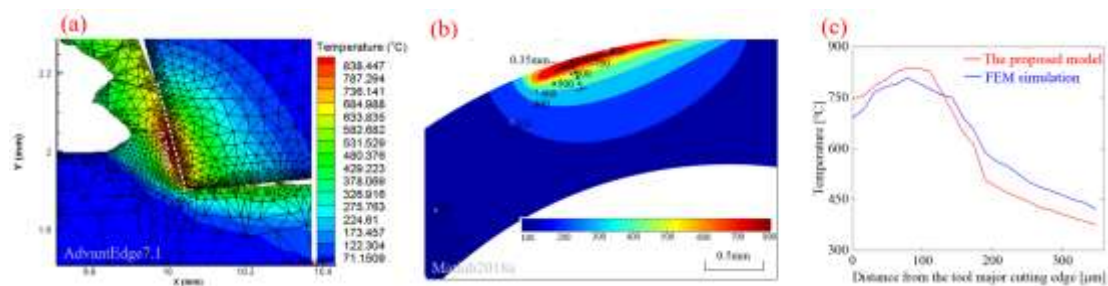


Fig. 4. Temperature distributions of experiment No. 1. ($a_p=0.5$ mm, $V_c=75$ m/min, $F_t=0.1$ mm/rev); (a) Result from FEM simulation; (b) Result from the proposed model; (c) Temperature profiles.

3.3 Determination of cutting parameters for obtaining the maximum cutting temperatures

Fig. 5 shows the crater wear profile of the tool rake face under the V_c of 120 m/min, a_p of 1 mm and F_t of 0.15 mm/rev. The crater wear profile was extracted from the widest wear area (see the yellow line in Fig. 5a). Fig. 5b displays a side view of the maximum wear profile. It is interesting to find that the trend of the wear depth and temperature from the major cutting edge are in good agreement. The maximum crater wear depth (represented by K_T) and width (represented by K_B) were defined along the longest tool chip contact length. The fitting data for experiment Nos. 1-9 were listed in Table 7. According to Ref. [31], the cutting inserts were declared worn out when the average flank wear width was 400 μm , or the maximum flank wear width was 700 μm , or the K_T was restricted to 140 μm .

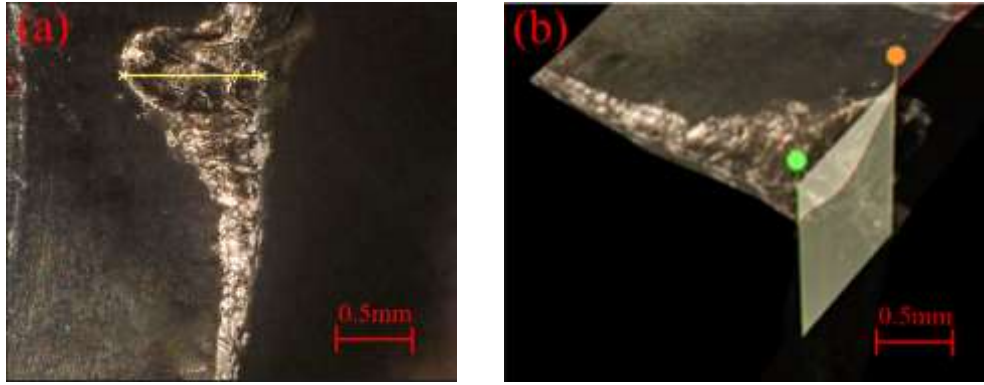


Fig. 5. Measurement of crater wear profile. (a) Aerial view; (b) Side view.

Table 7 The crater wear depth, width and the maximum temperature for experiment Nos. 1-9.

| No. | $K_T/\mu\text{m}$ | $K_B/\mu\text{m}$ | $T_{\text{max}}/^\circ\text{C}$ |
|-----|-------------------|-------------------|---------------------------------|
| 1 | 12 | 199 | 840 |
| 2 | 56 | 430 | 930 |
| 3 | 80 | 656 | 970 |
| 4 | 137 | 709 | 1013 |
| 5 | 57 | 450 | 939 |
| 6 | 143 | 677 | 1002 |
| 7 | 147 | 686 | 1007 |
| 8 | 188 | 823 | 1083 |
| 9 | 106 | 646 | 965 |

The data from experiments Nos. 1-9 were used to conduct ANOVA to determine the effects of various cutting parameters on crater wear. It is worth noting that the crater depth is used as the standard to judge whether the tool is invalid [16], so it is acceptable to analyze only the wear depth. As shown in Table 8, V_c is significant at 3.0% and hence has a major impact on crater wear depth. F_t is crucial at a 4.5% level and has a secondary influence. However, the influence of a_p on crater wear depth is not obvious. Consequently, a number of cutting parameters were selected with constant cutting depth to obtain different maximum temperatures (T_{max}) at the tool-chip interface. The selected cutting parameters were listed in Table 9.

Table 8 ANOVA results for crater wear depth.

| Factor | Sum of squares | Degrees of freedom | Mean sum of squares | F | Sig. |
|--------|----------------|--------------------|---------------------|-------|-------|
| a_p | 101.448 | 2 | 50.724 | 0.015 | 0.817 |
| V_c | 14669.073 | 2 | 7334.537 | 6.863 | 0.030 |
| F_t | 9700.234 | 2 | 4850.117 | 4.269 | 0.045 |
| Error | 453.252 | 2 | 226.626 | - | - |

Table 9 Cutting parameters.

| No. | a_p /mm | V_c /(m/min) | F_t /(mm/rev) |
|-----|-----------|----------------|-----------------|
| 10 | 0.5 | 80 | 0.1 |
| 11 | 0.5 | 110 | 0.1 |
| 12 | 0.5 | 90 | 0.125 |
| 13 | 0.5 | 90 | 0.175 |
| 14 | 0.5 | 120 | 0.125 |
| 15 | 0.5 | 105 | 0.15 |
| 16 | 0.5 | 105 | 0.175 |
| 17 | 0.5 | 75 | 0.125 |

4. Crater wear model considering temperature distribution

In this section, according to the previous fitting results, an experiment-based hypothesis was put forward considering the temperature distribution at the tool-chip interface. Further, a crater wear prediction model considering the effect of temperature was established through experimental results and analytical approaches.

4.1 Hypothesis of crater wear mechanism

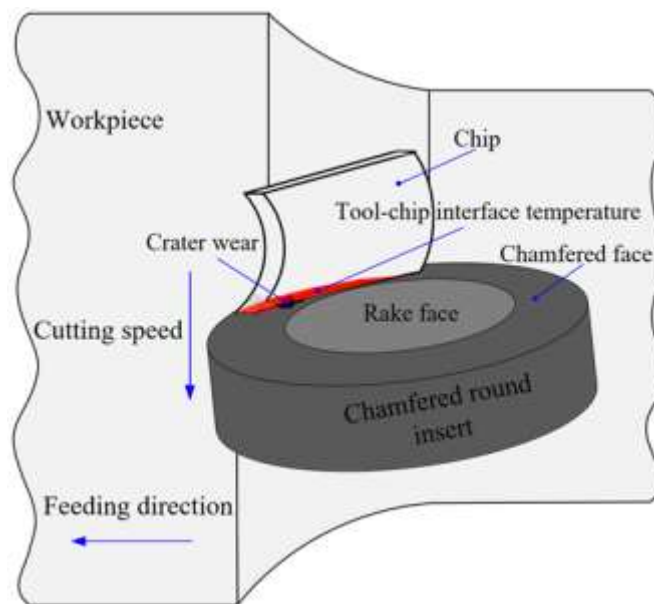


Fig. 6. Schematic diagram of the crater wear mechanism.

Fig. 6 demonstrates the 3D schematic diagram of the wear mechanism in turning operations. The maximum wear depth occurs very close to the position where the highest temperature appears at the tool-chip interface. It is in qualitative agreement with the observations of Ramírez [16], Dearnley [32] and Komanduri [33]. Fig. 7 shows the

crater wear with ceramic cutting inserts under various cutting conditions. From the figure, it can be observed that the crater areas marked with yellow circles are located at the tool-chip interface. The formation pattern of crater wear during machining processes is typically approximated as an arc [34-36], as shown in Fig. 8. It is interesting to find that the most serious crater wear occurs at the place with the greatest temperature in Fig. 8. This leads to a hypothesis that crater wear may be caused by temperature at the tool-chip interface. A quantitative relation between crater wear depth and temperature at the tool-chip interface, as well as crater wear width, will be presented in this section.

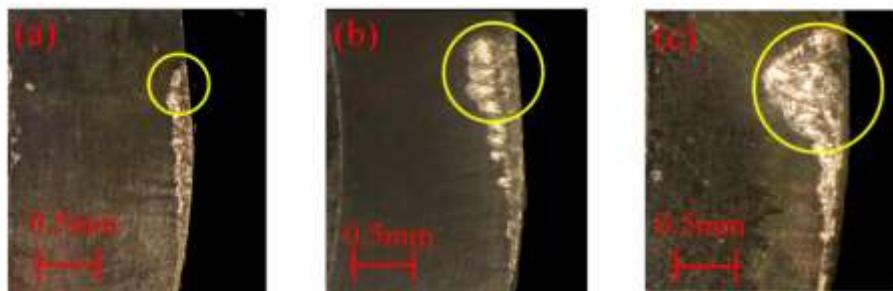


Fig. 7. The crater wear under various cutting conditions. (a) $a_p=0.5$ mm, $V_c=80$ m/min, $F_t=0.1$ mm/rev; (b) $a_p=0.5$ mm, $V_c=90$ m/min, $F_t=0.1$ mm/rev; (c) $a_p=1$ mm, $V_c=120$ m/min, $F_t=0.15$ mm/rev.

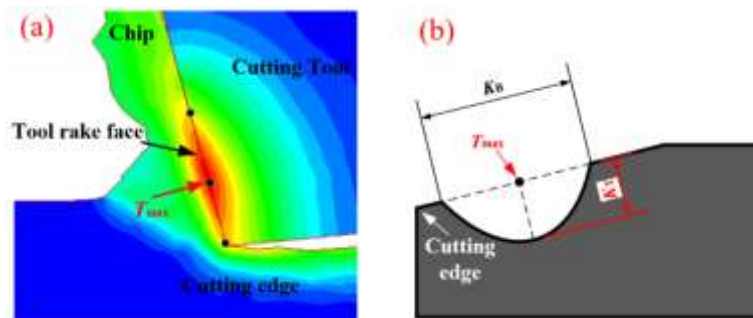


Fig. 8. Schematic diagram of temperature-wear relationship. (a) Temperature distribution of the cutting tool; (b) Schematic of crater wear geometry.

4.2 Crater wear formation and temperature profiles

The measurement of crater wear and the temperature distribution along the longest tool chip contact are shown in Figs. 9-16. Figs. 9-16a show the pictures of the crater wear profiles. The crater wear edges were detected by OriginPro using these figures. The profiles fitted by cubic polynomial curves accorded well with the measured data,

as shown in Figs. 9-16b. In Figs. 9-16b, the blue lines with circles represent the real profiles of crater wear measured from the tool cutting edge along the longest contact length, while red lines indicate the virtual wear profiles. The crater wear depth and width were determined using virtual profiles. Figs. 9-16c describe the temperature profiles at the cross-section perpendicular to the primary cutting edge and throughout the location of the K_T . In Figs. 9-16c, black triangles and red curves represent the calculation and the fitting temperature distributions respectively. The fitting temperature profiles with cubic polynomial curves were used to find the maximum cutting temperature and its location. Observing from Figs. 9-16b and c, the positions of the maximum wear depth and the highest temperature are very close for each case. The fitting data for K_T , K_B and T_{max} are listed in Table 10. Compared with Table 4, a comprehensive influence rule can be revealed. Based on the results of experiments Nos. 10-17, it can be observed that crater wear is not obvious when small cutting speeds are combined with small feed rates. Crater wear depth increases with the increase of cutting speed and feed rate. A linear relationship between T_{max} and K_B was derived by the fitting results in Table 10, as shown in Fig. 17.

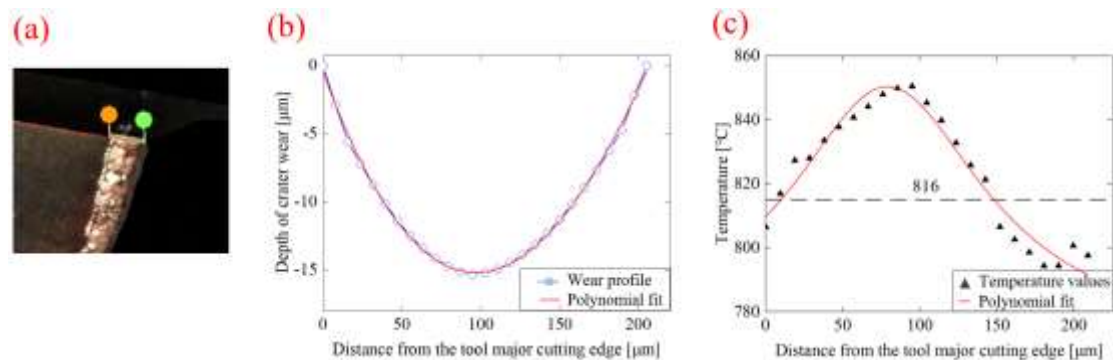


Fig. 9. Crater wear and temperature distribution of Experiment No. 10 ($a_p=0.5$ mm, $V_c=80$ m/min, $F_t=0.1$ mm/rev). (a) Wear picture; (b) Wear boundary; (c) Temperature profile.

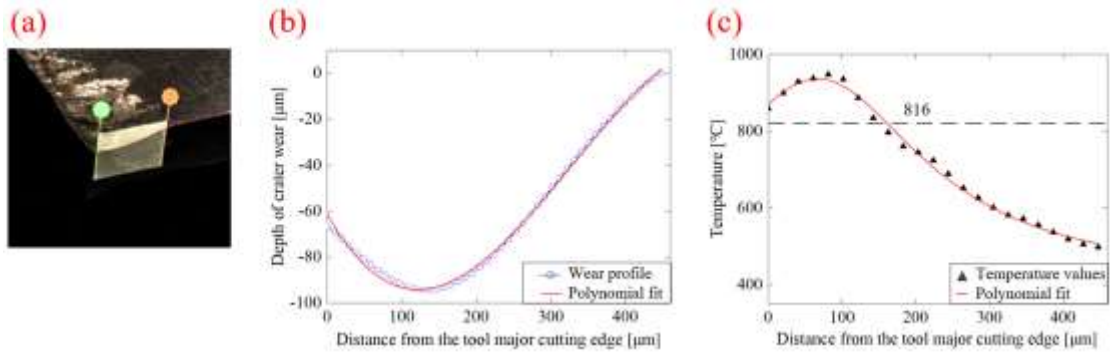


Fig. 10. Crater wear and temperature distribution of Experiment No. 11 ($a_p=0.5$ mm, $V_c=110$ m/min, $F_t=0.1$ mm/rev). (a) Wear picture; (b) Wear boundary; (c) Temperature profile.

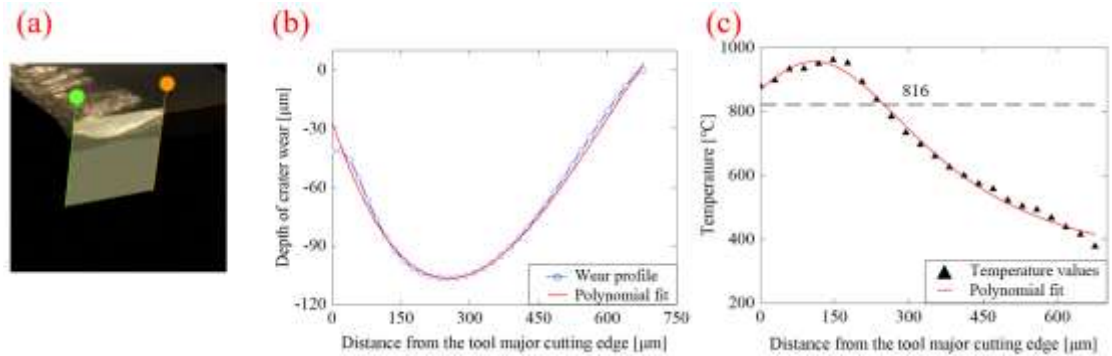


Fig. 11. Crater wear and temperature distribution of Experiment No. 12 ($a_p=0.5$ mm, $V_c=90$ m/min, $F_t=0.125$ mm/rev). (a) Wear picture; (b) Wear boundary; (c) Temperature profile.

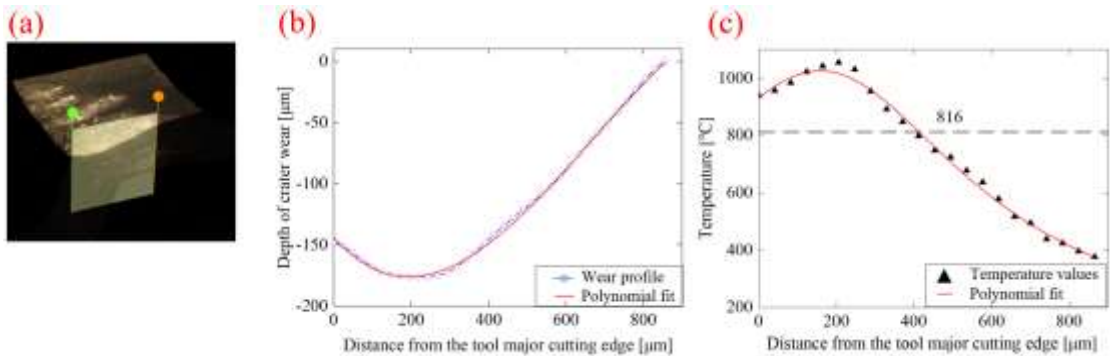


Fig. 12. Crater wear and temperature distribution of Experiment No. 13 ($a_p=0.5$ mm, $V_c=90$ m/min, $F_t=0.175$ mm/rev). (a) Wear picture; (b) Wear boundary; (c) Temperature profile.

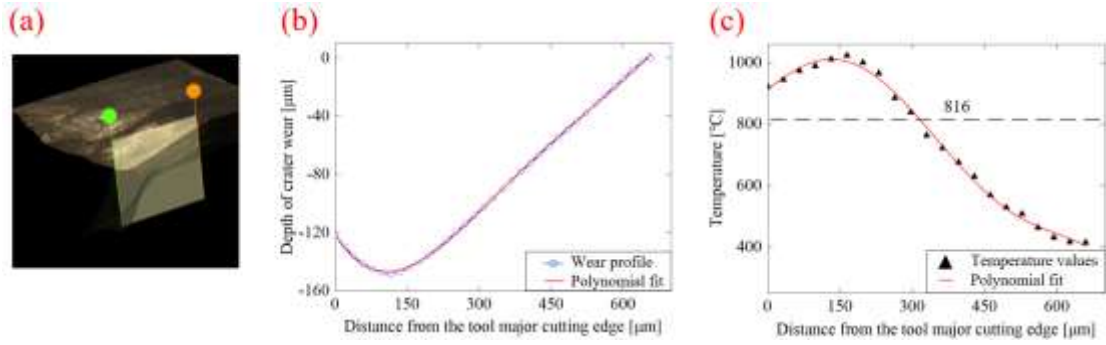


Fig. 13. Crater wear and temperature distribution of Experiment No. 14 ($a_p=0.5$ mm, $V_c=120$ m/min, $F_t=0.125$ mm/rev). (a) Wear picture; (b) Wear boundary; (c) Temperature profile.

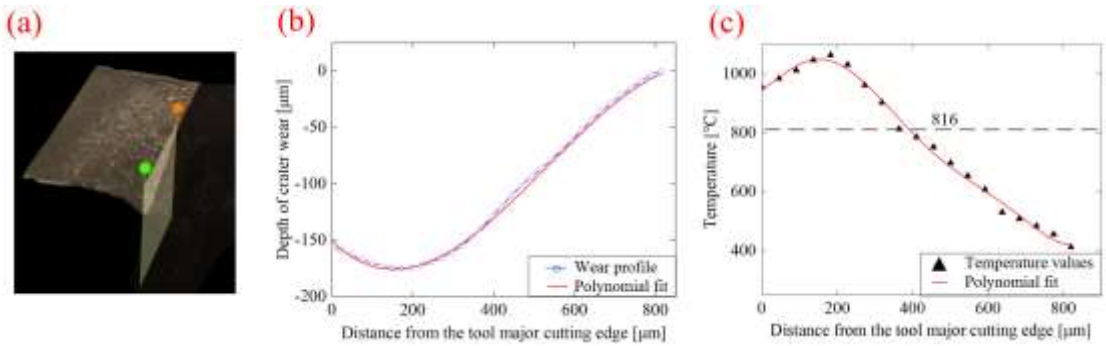


Fig. 14. Crater wear and temperature distribution of Experiment No. 15 ($a_p=0.5$ mm, $V_c=105$ m/min, $F_t=0.15$ mm/rev). (a) Wear picture; (b) Wear boundary; (c) Temperature profile.

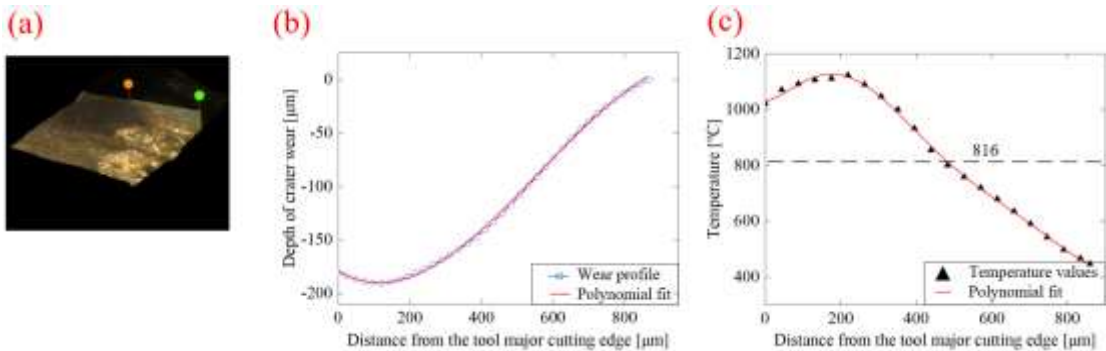


Fig.15. Crater wear and temperature distribution of Experiment No. 16 ($a_p=0.5$ mm, $V_c=105$ m/min, $F_t=0.175$ mm/rev). (a) Wear picture; (b) Wear boundary; (c) Temperature profile.

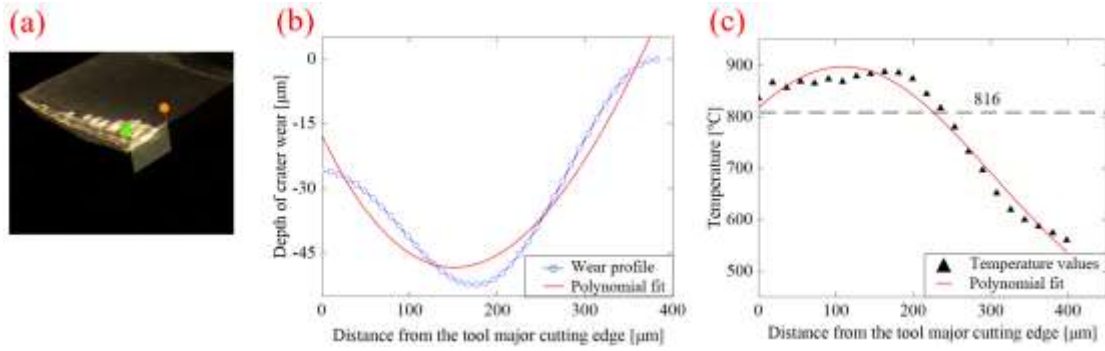


Fig. 16. Crater wear and temperature distribution of Experiment No. 17 ($a_p=0.5$ mm, $V_c=75$ m/min, $F_t=0.125$ mm/rev). (a) Wear picture; (b) Wear boundary; (c) Temperature profile.

Table 10 Fitting data for K_T , K_B and T_{max} of experiment Nos.10-17.

| No. | a_p /mm | V_c /(m/min) | F_t /(mm/rev) | K_T /μm | K_B /μm | T_{max} /°C |
|-----|-----------|----------------|-----------------|-----------|-----------|---------------|
| 10 | 0.5 | 80 | 0.1 | 15 | 205 | 850 |
| 11 | 0.5 | 110 | 0.1 | 88 | 449 | 947 |
| 12 | 0.5 | 90 | 0.125 | 106 | 679 | 962 |
| 13 | 0.5 | 90 | 0.175 | 176 | 856 | 1055 |
| 14 | 0.5 | 120 | 0.125 | 149 | 656 | 1024 |
| 15 | 0.5 | 105 | 0.15 | 174 | 815 | 1063 |
| 16 | 0.5 | 105 | 0.175 | 190 | 861 | 1124 |
| 17 | 0.5 | 75 | 0.125 | 52 | 394 | 887 |

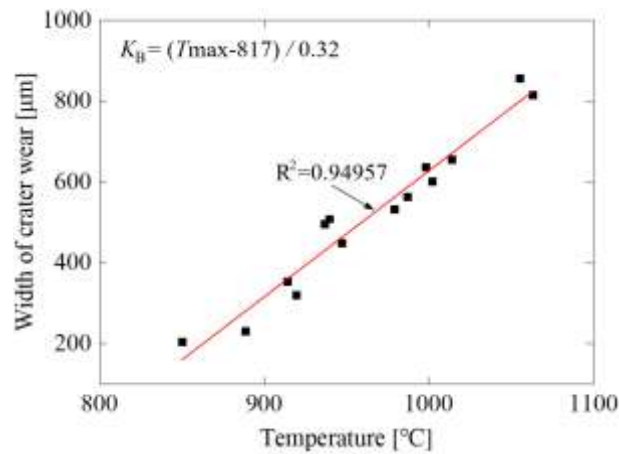


Fig. 17. The linear fit between the maximum temperature and crater wear width.

4.3 Crater wear model

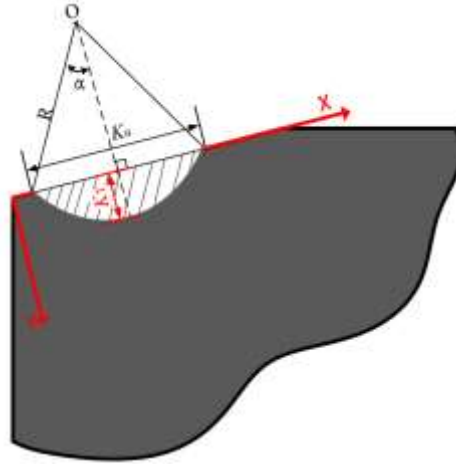


Fig.18. Schematic of the geometry of tool crater wear.

Based on the geometry of tool crater wear in Fig. 18, the relationship between K_B , K_T and radius R is as follow:

$$R^2 = \left(\frac{K_B}{2}\right)^2 + (R - K_T)^2 \quad (12)$$

Given K_B and K_T at a certain time, the radius R is calculated as:

$$R = \frac{\left(\frac{K_B}{2}\right)^2 + K_T^2}{2K_T} \quad (13)$$

Then the area of the shaded region (S) in Fig. 18 can be calculated by the following formula:

$$\begin{aligned} S &= \frac{2\alpha}{2\pi} \pi R^2 - \frac{1}{2} K_B R \cos \alpha \\ &= \alpha R^2 - \frac{1}{2} 2R \sin \alpha R \cos \alpha = R^2 (\alpha - \sin \alpha \cos \alpha) \end{aligned} \quad (14)$$

where

$$\alpha = \arcsin\left(\frac{K_B}{2R}\right) = \arcsin\left(\frac{K_T K_B}{\left(\frac{K_B}{2}\right)^2 + K_T^2}\right) \quad (15)$$

Furthermore, the area of the shaded region (S) can be extended as a function of K_B and K_T :

$$S = \left(\frac{A}{2K_T}\right)^2 \left(\arcsin\left(\frac{C}{A}\right) - \frac{BC}{A^2}\right) \quad (16)$$

where $A = \left(\frac{K_B}{2}\right)^2 + K_T^2$, $B = \left(\frac{K_B}{2}\right)^2 - K_T^2$ and $C = K_B K_T$. The condition $\frac{K_B}{2} > K_T$ is assumed in this study, which is suitable in turning Ti6Al4V.

Supposing the contact width is w , then the total volume loss can be determined by:

$$V_{\text{wear}} = wS = w \left(\frac{A}{2K_T}\right)^2 \left(\arcsin\left(\frac{C}{A}\right) - \frac{BC}{A^2}\right) \quad (17)$$

Assuming K_B remains unchanged with the development of tool wear under the same cutting conditions, the following relationship can be obtained by differentiation of V_{wear} to the variable K_T :

$$\frac{dV_{\text{wear}}}{dK_T} = w \frac{dS}{dK_T} = wD(K_T) \quad (18)$$

where

$$D(K_T) = \frac{AB}{2K_T^3} \left(\arcsin\left(\frac{C}{A}\right) - \frac{BC}{A^2}\right) - \frac{AK_B}{4K_T^2} - \frac{BK_B + 2CK_T}{4K_T^2} + \frac{BC}{AK_T} \quad (19)$$

Similarly, K_T is assumed to remain constant as temperature at the tool-chip interface increases under the same turning conditions, and by differentiation of V_{wear} to the variable K_B , the following relation is derived:

$$\frac{dV_{\text{wear}}}{dK_B} = w \frac{dS}{dK_B} = wD(K_B) \quad (20)$$

where

$$D(K_B) = \frac{AK_B}{2K_T^2} \left(\arcsin\left(\frac{C}{A}\right) - \frac{BC}{A^2}\right) + \frac{A}{4K_T} - \frac{BK_T - CK_B / 2}{4K_T^2} + \frac{BK_B^2}{4AK_T} \quad (21)$$

According to the chain rule, the K_T progress rate to the variable K_B can be written as follow:

$$\begin{aligned} \frac{dK_T}{dK_B} &= \frac{dV_{\text{wear}}}{dK_B} \bigg/ \frac{dV_{\text{wear}}}{dK_T} = \frac{D(K_B)}{D(K_T)} \\ &= \frac{\frac{AK_B}{2K_T^2} \left(\arcsin\left(\frac{C}{A}\right) - \frac{BC}{A^2}\right) + \frac{A}{4K_T} - \frac{BK_T - CK_B / 2}{4K_T^2} + \frac{BK_B^2}{4AK_T}}{\frac{AB}{2K_T^3} \left(\arcsin\left(\frac{C}{A}\right) - \frac{BC}{A^2}\right) - \frac{AK_B}{4K_T^2} - \frac{BK_B + 2CK_T}{4K_T^2} + \frac{BC}{AK_T}} \end{aligned} \quad (22)$$

Eq. (22) depicts the relation between K_T and K_B of the rake face.

As illustrated in Fig. 17, the relation of K_B with the maximum temperature value T_{max} on the rake face can be expressed as:

$$T_{\max}=817+0.32K_B \quad (23)$$

$$\frac{dK_T}{dT} = \frac{dK_T}{dK_B} \bigg/ \frac{dT}{dK_B} = 3.125 \frac{dK_T}{dK_B} \quad (24)$$

With the maximum temperature value and crater wear data from Table 10, the results can be estimated. According to the assumed linear relationship, the relation between K_T and T_{\max} can be written as

$$K_T = -N_0(T - T_0) + Q \quad (25)$$

where

$$N_0 = \frac{dK_T}{dT} \quad (26)$$

The average ratio can be calculated using the data from Table 10:

$$\bar{N}_0 = \frac{\sum N_{0i}}{n} = -0.68 \quad (27)$$

Then the relation between crater wear depth K_T (unit: μm) and the maximum temperature value T_{\max} (unit: $^{\circ}\text{C}$) can be further rewritten as:

$$K_T = 0.68(T_{\max} - 988) + 117 \quad (28)$$

This relationship is depicted in detail in Fig. 19. The figure shows that no crater wear appears when the maximum temperature value is restricted, and a crucial maximum temperature value (about 816 $^{\circ}\text{C}$) exists for the appearance of crater wear depth, as sector S in Fig. 19. The depth of crater wear increases with the increasing temperature when the temperature exceeds the critical value. It should be noted that the model is invalid when the temperature rises to the melting point of Ti6Al4V.

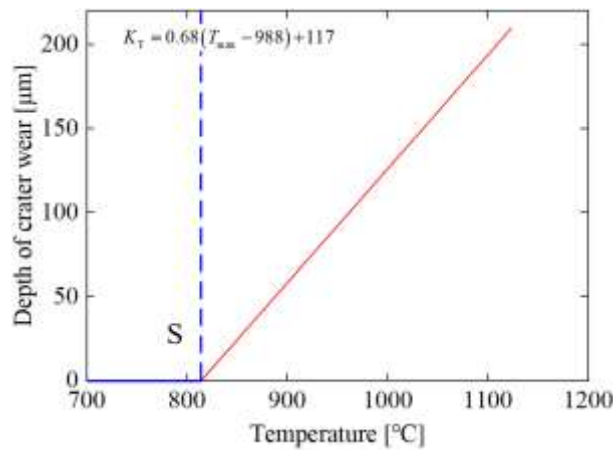


Fig. 19. The relation between crater wear depth and the maximum temperature.

5. Model verification and discussion

In this section, a set of cutting experiments were performed via dry turning of Ti6Al4V with ceramic tools to verify the effectiveness of the proposed crater wear prediction model. Then, the full study is discussed technically.

5.1 Model verification

Cutting experiments were carried out to validate the proposed crater wear prediction model. To verify that there is no obvious wear when the cutting temperature is small enough, an experiment was done with a set of small cutting parameters ($a_p=0.5$ mm, $F_t=0.1$ mm/rev, $V_c=60$ m/min). The experiment results are shown in Fig. 20. From the temperature distribution given in Fig. 20b, it can be obtained that the maximum temperature at the tool-chip interface is about 810 °C (less than the limitation value of 816 °C). No obvious crater wear was observed (see Fig. 20c). It indicates that no crater wear appears when the temperature is restricted, as region S illustrated in Fig. 19.

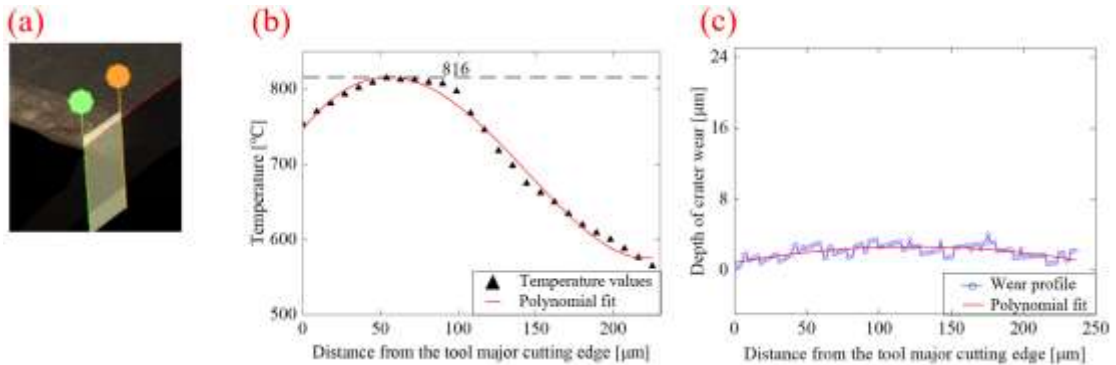


Fig. 20. Crater wear and temperature distribution with the cutting parameters below: $a_p=0.5$ mm, $F_t=0.1$ mm/rev, $V_c=60$ m/min. (a) Wear picture; (b) Temperature distribution; (c) Wear boundary.

As shown in Table 11, to validate the crater wear prediction model established in this paper, a series of cutting experiments under various conditions were conducted. The maximum temperatures of these experiments obtained from the proposed cutting temperature model are also listed in Table 11. The wear profiles and temperature distributions are shown in Figs. 21-23. The crater wear width and depth from fitting results and predictions with the proposed models are given in Fig. 24. From the figure, it can be seen that the predicted maximum wear depths and widths match quite well

with the measured results. The maximum error is roughly 12.6%, showing that the proposed model is workable.

Table 11 Verification experiment parameters and the maximum temperatures
(obtained from Figs. 21-23)

| No. | a_p /mm | V_c /(m/min) | F_t /(mm/rev) | T_{max} /°C |
|-----|-----------|----------------|-----------------|---------------|
| 18 | 0.5 | 90 | 0.1 | 889 |
| 19 | 0.5 | 120 | 0.1 | 987 |
| 20 | 0.5 | 120 | 0.15 | 1082 |

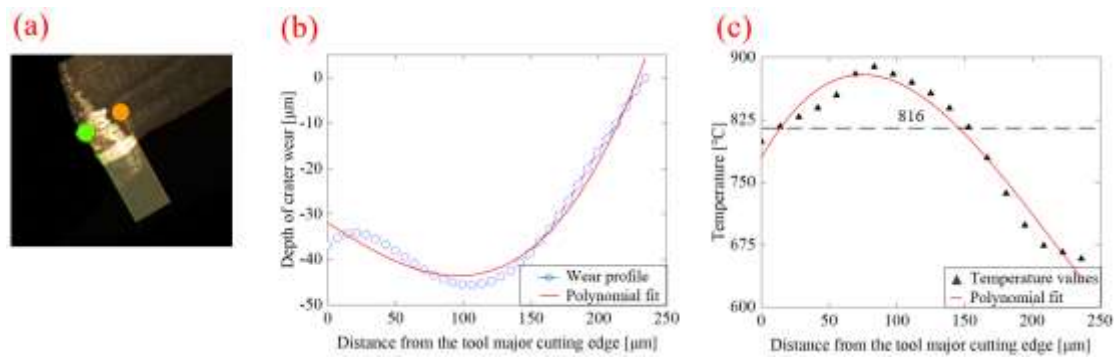


Fig. 21. Crater wear and temperature distribution of Experiment No. 18 ($a_p=0.5$ mm, $V_c=90$ m/min, $F_t=0.1$ mm/rev). (a) Wear picture; (b) Wear boundary; (c) Temperature distribution.

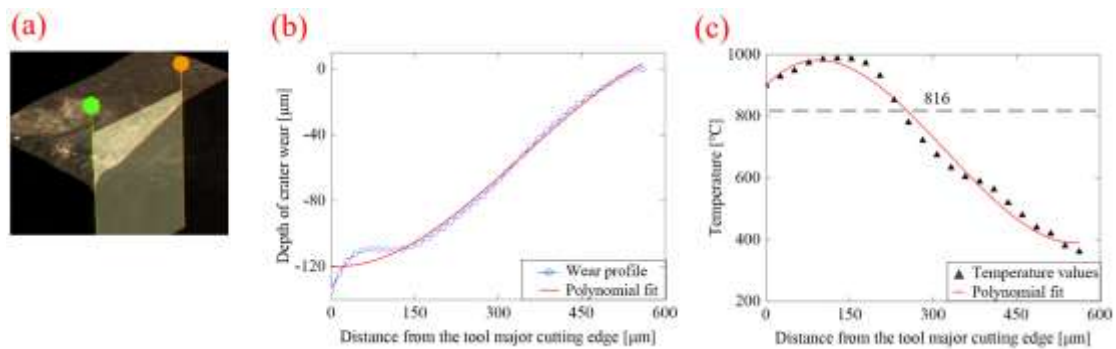


Fig. 22. Crater wear and temperature distribution of Experiment No. 19 ($a_p=0.5$ mm, $V_c=120$ m/min, $F_t=0.1$ mm/rev). (a) Wear picture; (b) Wear boundary; (c) Temperature distribution.

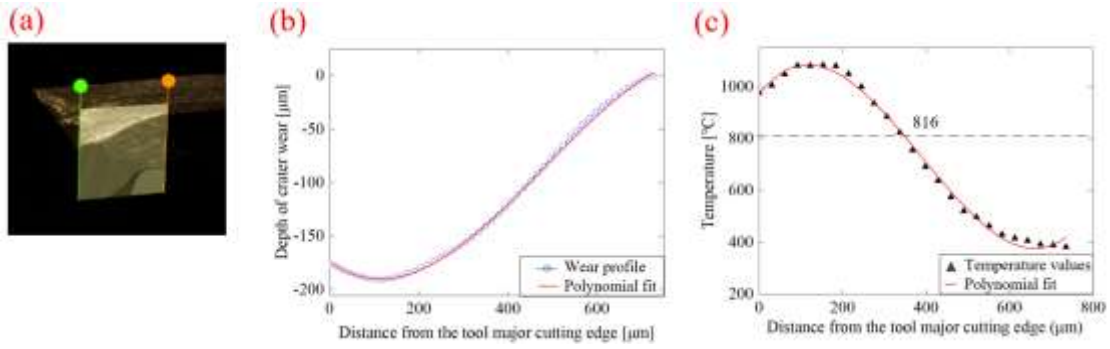


Fig. 23. Crater wear and temperature distribution of Experiment No. 20 ($a_p=0.5$ mm, $V_c=120$ m/min, $F_t=0.15$ mm/rev). (a) Wear picture; (b) Wear boundary; (c) Temperature distribution.

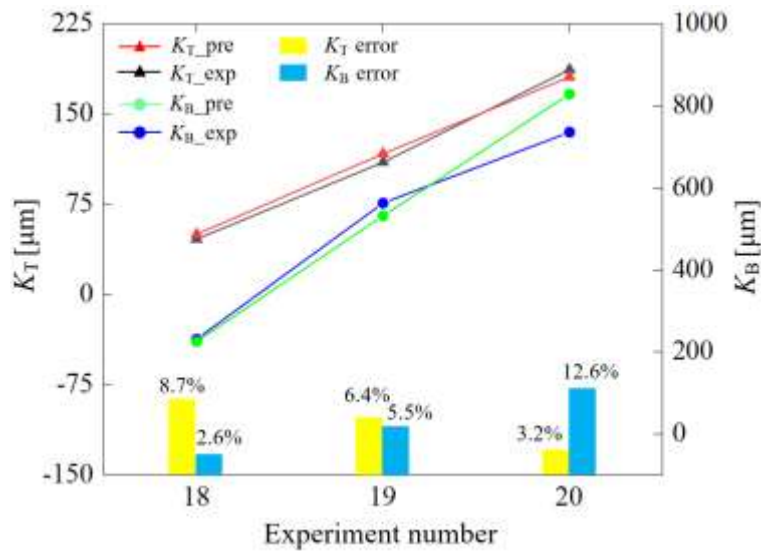


Fig. 24. Fitting results and predictions with the proposed models for crater wear depth and width of Experiment No. 18 ($a_p=0.5$ mm, $V_c=90$ m/min, $F_t=0.1$ mm/rev), No. 19 ($a_p=0.5$ mm, $V_c=120$ m/min, $F_t=0.1$ mm/rev) and No. 20 ($a_p=0.5$ mm, $V_c=120$ m/min, $F_t=0.15$ mm/rev), respectively.

5.2 Discussion

As shown in Figs. 9-16, both the temperature and crater wear profile first increase and then decrease along the longest contact from the main cutting edge of the tool. The positions where the maximum wear depth and the highest temperature appear are very close and the crater wear depth increases with increasing temperature and decreases with decreasing temperature. It indicates that the change trends of the temperature and crater wear profile are in good agreement, which meets the assumptions proposed in Section 4.1.

It is worth further discussing why observations from Figs. 9-16 appear. It is obviously noticed that the position of the highest temperature always appears near the tool major cutting edge, not anywhere else at the tool-chip interface. Fig. 25 clearly shows the variation trends of shear stress and chip flow velocity at the tool-chip interface. According to the theory of dual contact zone proposed by Zorev [37], there is a mixed friction characteristic on the contact surface between the tool and the chip. Fig. 25a shows that in the machining of metal processing, sticking friction first occurs and then changes to sliding friction along the contact length between the tool and the chip. These two kinds of friction dominate the tool-chip interface. The chip flow velocity near the tool major cutting edge is close to zero. With the increase of the distance from the tool major cutting edge, the chip flow velocity gradually increases, and finally reaches the maximum at the starting point of the sliding zone, and then remains unchanged as shown in Fig. 25b. The tendency of shear stress is completely opposite to that of chip flow velocity. Firstly, the shear stress starts at the maximum value and gradually decreases from the starting point of the sliding zone until it becomes zero as given in Fig. 25b. At the junction of sticking zone and sliding zone, the chip flow velocity and shear stress of the cutting element reach the maximums simultaneously. According to Eq. (1) in section 3.1, the heat source intensity reaches the maximum, which eventually leads to the maximum temperature at this position. High temperature promotes diffusion and softening of the material on the tool surface, which accelerates crater wear [8-12]. It can be found the higher the temperature is, the more serious the crater wear is. The above discussion further confirms the hypothesis proposed in this paper.

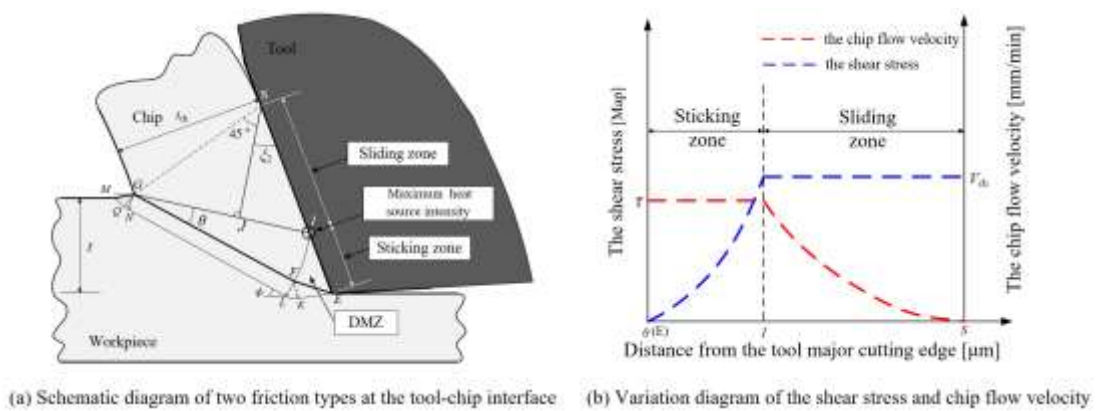


Fig. 25. Schematic diagram of shear stress and chip flow velocity at the tool-chip interface based on Zorev's dual contact zone theory [37].

According to the analysis in Section 3.3, the crater wear depth is affected differently by cutting parameters. Based on the crater wear prediction model proposed in this paper, the effect of the combination of different cutting parameters on the crater wear is discussed. Fig. 26 shows the maximum temperature T_{\max} at the tool-chip interface and the maximum depth of crater wear K_T with respect to V_c and F_t . Fig. 26a depicts the increasing trend of T_{\max} and K_T with increasing V_c . The tendencies of T_{\max} and K_T with increasing F_t are given in Fig. 26b. It can be seen that these two machining parameters have positive effects on T_{\max} and K_T . It is also observed that the growing tendency slows down when the cutting speed reaches 105 m/min and the feed rate approaches 0.15 mm/rev. This might be attributed to the thermal-softening effect when the cutting temperature reaches extremely high levels.

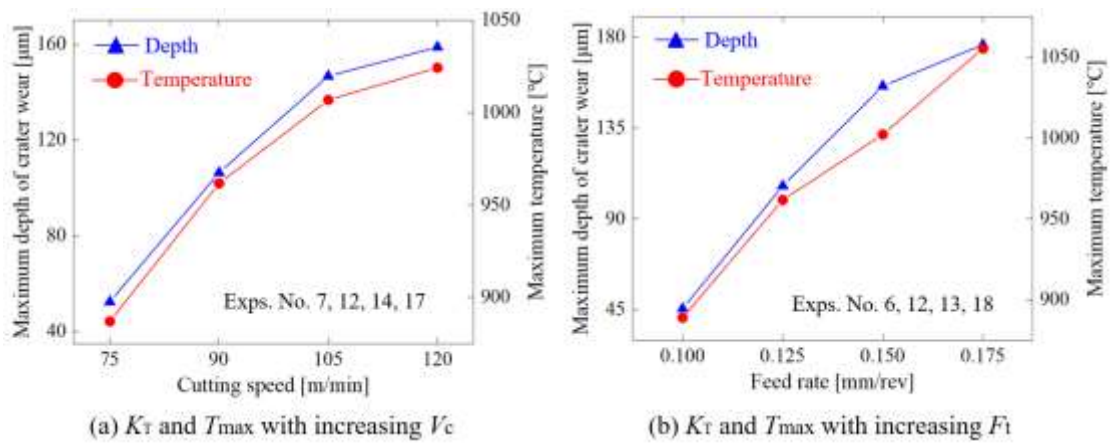


Fig. 26. The maximum depth of crater wear (K_T) and the maximum temperature (T_{\max}) under different cutting parameters. (a) the cutting depth and feed rate remain constant ($a_p=0.5$ mm, $F_t=0.125$ mm/rev); (b) the cutting depth and cutting speed remain constant ($a_p=0.5$ mm, $V_c=90$ mm/rev).

The most important influencing factor is cutting speed, according to the ANOVA result. Cutting temperature increases as cutting speed increases from 75 m/min to 120 m/min when other machining parameters remain constant. When cutting speed is sufficiently small, no evident crater wear occurs due to low cutting temperature (such as Nos. 1 and 10). For some large cutting speeds (such as Nos. 19 and 20), crater wear can easily form and even collapsed edges can occur as the high cutting temperature softens the tool. Observing from Fig. 26b, it is found that feed rate has a vital influence on crater wear. Cutting temperatures increase with the increasing of feed rate when the cutting depth and speed stay constant. According to the ANOVA result, cutting depth

has a slight effect on crater wear compared with cutting speed and feed rate. For the reason that too low cutting speed will cause very large vibration during turning, cutting speed should not be too low. Consequently, a combination of large feed rate, large cutting depth and medium cutting speed is recommended for increasing tool life and improving machining efficiency.

6. Conclusions

In this work, a study is conducted to quantitatively elaborate the crater wear in turning of Ti6Al4V alloy. A crater wear depth and width prediction model considering the cutting temperature distribution at the tool-chip interface is proposed. In addition, a quantitative analysis of the relationship between the maximum cutting temperature at the tool-chip interface and the maximum crater wear depth as well as width is carried out. The investigation is an attempt to quantitatively describe the crater wear during difficult-to-cut metal machining. The major contributions can be concluded as follows:

(1) A novel crater wear prediction model has been developed to demonstrate the relationship between K_T and T_{max} . According to the proposed model, no crater wear occurs when the maximum temperature is restricted, and the depth and width of crater wear increase as the maximum temperature increases.

(2) The good agreement between experimental and predicted results over a broad range of cutting parameters indicates that the crater wear depth and width prediction model is feasible.

(3) Cutting speed has a strong effect on K_T and K_B , followed by feed rate. In general, K_T and K_B increase with increasing V_c and F_t . Besides, a_p has a negligible effect on K_T and K_B . A combination of large feed rate, large cutting depth and medium cutting speed can be used to decrease crater wear and improve machining efficiency in turning.

Author contribution The ranking of the authors in the manuscript has been sorted according to their contributions. All the authors have approved the ranking of authors and the affiliation of the corresponding author.

Funding This work was financially supported by the Guangdong Major Project of Basic and Applied Basic Research (2021B0301030001), National Natural Science Foundation of China (52175482), Hubei Province Natural Science Foundation of China (2021CFB304) and the State Key Laboratory of Digital Manufacturing Equipment and Technology (DMETKF2021005, DMETKF2021022).

Availability of data and material The data in this study is obtained or measured through the corresponding experiments, and the materials have been given in this paper. They can be used as a reference for the related researchers.

Declarations

Ethics approval Not applicable.

Consent to participate All the authors listed have participated in the preparation of the manuscript and the related experiments.

Consent for publication This manuscript is approved by all the authors for publication. It is the original research that has not been published previously, and not under consideration for publication elsewhere, in whole or in part.

Competing interests The authors declare no competing interests.

References

- [1] Hou G, Li A, Song X, Zhao J (2018) Effect of cutting parameters on surface quality in multi-step turning of Ti-6Al-4V titanium alloy. *Int J Adv Manuf Technol* 98(5): 1355-1365.
- [2] Ezugwu EO, Wang ZM (1997) Titanium alloys and their machinability—a review. *J Mater Process Technol* 68(3):262-274.
- [3] Venugopal KA, Paul S, Chattopadhyay AB (2007) Growth of tool wear in turning

- of Ti-6Al-4V alloy under cryogenic cooling. *Wear* 262(9-10):1071-1078.
- [4] Mishra SK, Talwar D, Singh K, Chopra A, Ghosh S, Aravindan S (2021) Micromechanical characterization and dynamic wear study of DC-arc coated cemented carbide cutting tools for dry titanium turning. *Ceram Int* 47(22):31798-31810.
- [5] Hosseini A, Kishawy HA (2014) Cutting tool materials and tool wear, *Machining of Titanium Alloys, Materials Forming. Machining and Tribology*. Springer, Berlin, Heidelberg, pp 31-56.
- [6] Liang L, Liu X, Li X, Li YY (2015) Wear mechanisms of WC-10Ni3Al carbide tool in dry turning of Ti6Al4V. *Int J Refract Met H* 48:272-285.
- [7] Zhang S, Li JF, Sun J, Jiang F (2010) Tool wear and cutting forces variation in high-speed end-milling Ti-6Al-4V alloy. *Int J Adv Manuf Technol* 46(1):69-78.
- [8] Hua J, Shivpuri R (2005) A cobalt diffusion based model for predicting crater wear of carbide tools in machining titanium alloys. *J Eng Mater Technol* 127(1):136-144.
- [9] Jawaid A, Sharif S, Koksai S (2000) Evaluation of wear mechanisms of coated carbide tools when face milling titanium alloy. *J Mater Process Technol* 99(1-3):266-274.
- [10] Bai D, Sun J, Chen W, Du D (2016) Molecular dynamics simulation of the diffusion behaviour between Co and Ti and its effect on the wear of WC/Co tools when titanium alloy is machined. *Ceram Int* 42(15):17754-17763.
- [11] Zhang S, Li JF, Deng JX, Li Y (2009) Investigation on diffusion wear during high-speed machining Ti-6Al-4V alloy with straight tungsten carbide tools. *Int J Adv Manuf Technol* 44(1):17-25.
- [12] Rahman Rashid RA, Palanisamy S, Sun S, Dargusch MS (2016) Tool wear mechanisms involved in crater formation on uncoated carbide tool when machining Ti6Al4V alloy. *Int J Adv Manuf Technol* 83(9):1457-1465.
- [13] Usui E, Shirakashi T, Kitagawa T (1984) Analytical prediction of cutting tool wear. *Wear* 100(1-3):129-151.
- [14] Malakizadi A, Gruber H, Sadik I, Nyborg L (2016) An FEM-based approach for tool wear estimation in machining. *Wear* 368:10-24.
- [15] Thepsonthi T, Özel T (2013) Experimental and finite element simulation based investigations on micro-milling Ti-6Al-4V titanium alloy: Effects of CBN coating on tool wear. *J Mater Process Technol* 213(4):532-542.

- [16] Ramírez F, Soldani X, Loya J, Miguélez H (2017) A new approach for time-space wear modeling applied to machining tool wear. *Wear* 390:125-134.
- [17] Norihiko N (2002) High-speed machining of titanium alloy. *Chin J Mech Eng-EN* 15:109-114.
- [18] Molinari A, Nouari M (2002) Modeling of tool wear by diffusion in metal cutting. *Wear* 252(1-2):135-149.
- [19] Wang K, Sun J, Du D, Chen W (2017) Quantitative analysis on crater wear of cemented carbide inserts when turning Ti-6Al-4V. *Int J Adv Manuf Technol* 91(1):527-535.
- [20] Sun J, Liao X, Yang S, Chen W (2019) Study on predictive modeling for thermal wear of uncoated carbide tool during machining of Ti-6Al-4V. *Ceram Int* 45(12):15262-15271.
- [21] Sartori S, Moro L, Ghiotti A, Bruschi S (2017) On the tool wear mechanisms in dry and cryogenic turning additive manufactured titanium alloys. *Tribol Int* 105:264-273.
- [22] Komanduri R, Hou ZB (2001) A review of the experimental techniques for the measurement of heat and temperatures generated in some manufacturing processes and tribology. *Tribol Int* 34(10):653-682.
- [23] Merchant ME (1945) Mechanics of the metal cutting process. I. Orthogonal cutting and a type 2 chip. *J Appl Phys* 16(5):267-275.
- [24] Zhuang K, Fu C, Weng J, Hu C (2021) Cutting edge microgeometries in metal cutting: A review. *Int J Adv Manuf Technol* 116(7):2045-2092.
- [25] Zhuang K, Hu C, Weng J, Zhang X, Ding H (2021) Three-dimensional temperature prediction in cylindrical turning with large-chamfer insert based on a modified slip-line field approach. *Chin J Aeronaut* 34(10):265-281.
- [26] Hu C, Zhuang K, Weng J, Zhang X, Ding H (2020) Cutting temperature prediction in negative-rake-angle machining with chamfered insert based on a modified slip-line field model. *Int J Mech Sci* 167:105273.
- [27] Hu C, Zhuang K, Weng J, Zhang X (2019) Thermal-mechanical model for cutting with negative rake angle based on a modified slip-line field approach. *Int J Mech Sci* 164:105167.
- [28] Weng J, Zhuang K, Zhu D, Guo S, Ding H (2018) An analytical model for the prediction of force distribution of round insert considering edge effect and size effect. *Int J Mech Sci* 138:86-98.

- [29] Huang Y, Liang SY (2005) Cutting temperature modeling based on non-uniform heat intensity and partition ratio. *Mach Sci Technol* 9(3):301-323.
- [30] Du M, Cheng Z, Wang S, Zhang Y (2019) Effects of damage evolution on simulation results of high speed machining Ti6Al4V. *Acta Aeronautica et Astronautica Sinica (in Chinese)* 40(7):422787.
- [31] Zhuang K, Zhu D, Zhang X, Ding H (2014) Notch wear prediction model in turning of Inconel 718 with ceramic tools considering the influence of work hardened layer. *Wear* 313(1-2):63-74.
- [32] Dearnley PA, Grearson AN (1986) Evaluation of principal wear mechanisms of cemented carbides and ceramics used for machining titanium alloy IMI 318. *Mater Sci Technol* 2(1):47-58.
- [33] Komanduri R (1982) Some clarifications on the mechanics of chip formation when machining titanium alloys. *Wear* 76(1):15-34.
- [34] Huang Y, Liang SY (2003) Cutting forces modeling considering the effect of tool thermal property—application to CBN hard turning. *Int J Mach Tools Manuf* 43(3):307-315.
- [35] Huang Y, Dawson TG (2005) Tool crater wear depth modeling in CBN hard turning. *Wear* 258(9):1455-1461.
- [36] Fang XD, Jawahir IS (1993) The effects of progressive tool wear and tool restricted contact on chip breakability in machining. *Wear* 160(2):243-252.
- [37] Zorev NN (1963) Inter-relationship between shear processes occurring along tool face and shear plane in metal cutting. *Int Res Prod Eng* 49:143–152.